

1           **Limited transferrin receptor clustering allows rapid**  
2           **diffusion of canine parvovirus into clathrin endocytic**  
3                           **structures**

4  
5  
6 David K. Cureton<sup>1</sup>, Carole E. Harbison<sup>2¶</sup>, Emmanuele Cocucci<sup>1</sup>, Colin R. Parrish<sup>2#</sup>, and Tomas  
7 Kirchhausen<sup>1#</sup>

8  
9 1) Immune Disease Institute and Program in Cellular and Molecular Medicine at Children's  
10 Hospital Boston, Boston, MA, USA

11 2) Baker Institute for Animal Health, College of Veterinary Medicine, Cornell University, Ithaca,  
12 NY, USA

13 ¶ Current address: Division of Comparative Pathology, New England Primate Research Center,  
14 Harvard Medical School, Southborough, MA 01772

15

16 \*co-corresponding authors

17 kirchhausen@crystal.harvard.edu

18 [crp3@cornell.edu](mailto:crp3@cornell.edu)

19

20 Running title: Clathrin-dependent parvovirus uptake

21 Abstract word count: 156

22 Text word count: 6291

23  
24  
25  
26  
27  
28  
29  
30  
31  
32  
33  
34  
35  
36  
37  
38  
39  
40  
41  
42  
43  
44  
45

## ABSTRACT

Viral pathogens usurp cell surface receptors to access clathrin endocytic structures, yet the mechanisms of virus incorporation into these structures remain incompletely understood. Here, we used fluorescence microscopy to directly visualize the association of single canine parvovirus (CPV) capsids with cellular transferrin receptors (TfR) on the surface of live feline cells and to monitor how these CPV-TfR complexes access endocytic structures. We found that most capsids associated with fewer than five TfRs, and that ~25% of TfR-bound capsids laterally diffused into assembling clathrin-coated pits less than 30 s after attachment. Capsids that did not encounter a coated pit dissociated from the cell surface with a half-life of ~30 s. Together, our results show how CPV exploits the natural mechanism of TfR endocytosis to engage the clathrin endocytic pathway and reveal that the low affinity of capsids for feline TfRs limits the residence time of capsids on the cell surface and thus the efficiency of virus internalization.

## INTRODUCTION

46

47 Animal viruses exploit cellular endocytic pathways to invade target cells. Virus particles  
48 engage these pathways by binding cell surface receptor molecules that facilitate virus  
49 endocytosis. These viral receptors include a wide variety of transmembrane proteins that  
50 normally function in the endocytosis of physiological ligands as well as other proteins and  
51 glycolipids without known endocytic functions. Although the primary receptors and pathways  
52 utilized by some viruses are now well-defined (30), the mechanisms by which receptors direct  
53 virus uptake by a given endocytic structure or pathway remain poorly understood.

54 Canine parvovirus (CPV) is a nonenveloped virus that utilizes the cellular transferrin  
55 receptor type I (TfR) to bind, enter, and infect target cells (33). In nature, CPV is a pathogen of  
56 dogs, cats, and related hosts (36). The viral host range is strain-specific and primarily dictated by  
57 the affinity of capsids for TfRs expressed on host cells (18, 19). CPV particles measure 26 nm in  
58 diameter and consist of an icosahedral capsid that packages the ~5 kb ssDNA genome (47). CPV  
59 binds to the TfR via raised regions that project from the three-fold axes of capsid symmetry (14),  
60 and cells internalize the receptor-bound capsids by clathrin-dependent endocytosis (34). Capsids  
61 then penetrate endosomal compartments and deliver the viral genome to the nucleus to initiate  
62 replication (15).

63 The TfR is a type II, homodimeric transmembrane glycoprotein that delivers iron into  
64 cells by binding and internalizing iron-loaded transferrin (Tf) (46). The butterfly-shaped receptor  
65 ectodomain spans ~11 nm and consists of three subdomains (23). Tf binds to residues in the  
66 membrane proximal protease-like domain and the central helical domain (4), while CPV capsids  
67 contact residues in the membrane distal apical domain (12, 32). Structural modeling of CPV-TfR  
68 interactions suggested that a single capsid can bind up to 24 TfRs, but biochemical and cryo-

69 electron microscopic analysis indicated that CPV capsids bind fewer than 7 TfR ectodomains in  
70 solution (14). It is currently unknown whether capsids cluster TfRs on the surface of target cells.

71 Cells internalize TfRs by clathrin-dependent endocytosis (3). This endocytic mechanism  
72 forms membrane vesicles that measure 40-120 nm in diameter and function to transport cargos  
73 from the cell surface to early endosomes (6, 21). Clathrin endocytic structures initiate upon  
74 clathrin recruitment to the plasma membrane by AP-2 adaptor complexes. Continued clathrin  
75 assembly invaginates the associated membrane to form a coated pit. Adaptor proteins within the  
76 assembling coated pits sequester cargos at the endocytic site by engaging the cytosolic domains  
77 of transmembrane receptor proteins, including those of the TfR (5, 45). The cargo-loaded pits  
78 then pinch off from the plasma membrane as coated vesicles, and the coat containing clathrin and  
79 the adaptors is rapidly disassembled to allow vesicle fusion with an endosome. Studies of  
80 clathrin-dependent endocytosis in live cells have shown that coated pits constitutively initiate on  
81 the cell surface and typically mature into coated vesicles within 30-90 s (10, 26, 41).

82 Numerous viruses utilize the clathrin endocytic pathway to enter host cells, yet the  
83 molecular events that govern virus incorporation into clathrin endocytic structures have not been  
84 characterized in detail. In this study, we imaged CPV entry with high temporal and spatial  
85 precision to dissect how CPV-TfR interactions influence the rate, efficiency, and mechanism of  
86 CPV incorporation into clathrin endocytic structures. Our analysis showed that CPV capsids  
87 bound to a low number of TfRs on the surface of live cells and rapidly engaged forming clathrin  
88 structures by a diffusion-based mechanism. Moreover, we found that capsids had a relatively  
89 short residence time on the cell surface, which in turn, limited the efficiency of capsid  
90 internalization.

91

92

**MATERIALS AND METHODS****93 Cells and viruses**

94 Feline kidney CRFK cells (7) were maintained at 37°C and 5% CO<sub>2</sub> in a 1:1 mixture of  
95 McCoy's 5A and Liebovitz L15 media (Mediatech, Inc.; Manassas, VA) supplemented with 5%  
96 fetal bovine serum (FBS) (Tissue Culture Biologicals; Tulare, CA). Chinese hamster ovary cells  
97 lacking the hamster TfR (TRVb cells) (29) were maintained under similar conditions in Ham's  
98 F-12 Nutrient Mixture (Mediatech) containing 5% FBS (Tissue Culture Biologicals). CRFK and  
99 TRVb cells were transfected with plasmid DNA encoding the rat  $\sigma$  subunit of the AP-2 complex  
100 C-terminally tagged with eGFP ( $\sigma$ 2-eGFP) (10). Plasmid-containing cells were selected with 0.5  
101 (CRFK) or 0.75 (TRVb) mg/mL Geneticin (G418) (Invitrogen Corporation; Carlsbad, CA), and  
102 clones that expressed low levels of  $\sigma$ 2-eGFP were isolated. TRVb cells were transfected with  
103 plasmids encoding the wt feline TfR (Genbank accession #AF276984.1) tagged with eGFP  
104 (fTfR-eGFP; see below for construction details) and selected in media containing 0.75 mg/mL  
105 G418. Cell transfections were performed with FuGENE HD according to the manufacturer's  
106 (Roche Diagnostics; Indianapolis, IN) instructions, and selected populations of transfected cells  
107 were maintained in media containing 0.4 mg/mL G418. For transient transfections of TRVb cells  
108 stably expressing  $\sigma$ 2-eGFP with plasmids encoding fTfR-mCherry, cells were plated on 25 mm  
109 glass coverslips and transfected as above ~20 h after plating. Cells expressing low levels of  
110 fTfR-mCherry were imaged ~18 h after transfection.

111 Viruses were recovered from the infectious plasmid clone of CPV-2 (CPV-d) (35) in  
112 NLFK feline kidney cells, a derivative of CRFK cells. Virus capsids were concentrated by  
113 polyethylene glycol precipitation followed by sucrose gradient centrifugation, which separated  
114 the full (DNA containing) and empty capsids. Purified capsids were dialyzed against either PBS

115 or 20 mM Tris-HCl (pH 7.5) and stored at 4°C (1). All imaging experiments were performed  
116 with empty capsids.

#### 117 **Fluorescently labeled virus**

118 Purified capsids were labeled with Alexa Fluor 647 (Invitrogen) (16), Atto 647N NHS, or  
119 Atto 568N NHS (Sigma-Aldrich Inc.; St. Louis, MO) in PBS for 30 min at room temperature  
120 using ~20% of the dye concentration recommended by the manufacturer. Labeled capsids were  
121 separated from free dye by passage through a Sephadex G25 column (GE Healthcare;  
122 Piscataway, NJ) in PBS, and eluted capsids were stored at 4°C. The number of dye molecules per  
123 capsid ranged from 6-10 for Alexa 647 and 3-6 for Atto 647, as measured spectroscopically  
124 (Alexa) or by capsid photobleaching analysis (Atto).

#### 125 **Plasmid construction**

126 The expression plasmids encoding fTfR-eGFP and fTfR-mCherry were generated as  
127 follows: (i) the wt feline TfR gene was PCR amplified from an existing pcDNA3.1(-) expression  
128 vector (33) using primers that contained restriction enzyme recognition sites for EcoRI (forward  
129 primer: 5'-GTCAGAATTCATGATGGATCAAGCCAGATC-3') or AgeI (reverse primer: 5'-  
130 GACTACCGGTGGATCCCCAACTCATTGTCAATATCCCCAAATGTC - 3'); (ii) the PCR  
131 product and peGFP-N1 (Clontech Laboratories, Inc.; Mountain View, CA) or an otherwise  
132 identical plasmid encoding mCherry in place of eGFP were digested with EcoRI and AgeI, and  
133 the cleaved DNA fragments were ligated to generate pTfR-eGFP. This cloning strategy  
134 introduced a 7 amino acid linker (GDPPVAT) between the TfR and the fluorescent protein open  
135 reading frame. The pAcGP67A baculovirus transfer vector encoding non-glycosylated (N413D,  
136 N611D) human transferrin with an N-terminal secretion signal followed by a hexahistidine tag  
137 (6His-Tf) was a kind gift of Dr. Pamela Bjorkman (California Institute of Technology; Pasadena,

138 CA). Site-directed mutagenesis was used to introduce a single cysteine residue between the  
139 secretion signal and histidine tag, and the presence of the introduced cysteine was confirmed by  
140 sequence analysis. The plasmid encoding eGFP with a C-terminal hexahistidine tag (eGFP-6His)  
141 was a kind gift of Dr. Massimo Merighi (Laboratory of Stephen Lory, Harvard Medical School).

#### 142 **Production of recombinant fluorescent proteins**

143 Baculoviruses expressing 6His-Tf were generated in *Spodoptera frugiperda* Sf9 cells  
144 using the BD BaculoGold Transfection Kit (BD Biosciences; San Diego, CA), and the  
145 recombinant protein was produced in *Trichoplusia ni* Hi5 cells. Secreted 6His-Tf was isolated  
146 from the cell supernatant using TALON Metal Affinity Resin (Clontech). Isolated protein was  
147 eluted using 200 mM imidazol in PBS to a final concentration of 0.54  $\mu$ M. Purified protein was  
148 labeled under non-reducing conditions with Atto 647N maleimide (Sigma-Aldrich) using a 4-  
149 fold molar excess of dye to protein for 1 h at room temperature. Labeled protein was separated  
150 from free dye using a G25 MicroSpin gel filtration column (GE Healthcare) and stored in PBS  
151 supplemented with 20% glycerol at -80°C. Spectroscopic analysis showed that ~80% of 6His-Tf  
152 molecules were labeled with dye.

153 eGFP-6His was expressed in *E. coli* strain BL21 grown in LB medium containing 100  
154  $\text{mg}^{-1}$  ampicilin at 37°C to an optical density of 0.6 at 600 nm. Expression of eGFP-6His was  
155 induced with 0.5 mM IPTG, and the cells were grown for 3 hrs at 37 °C. Cells were harvested by  
156 centrifugation (Sorvall RC3B rotor, 5000 rpm, 10 min, 4 °C) and resuspended in ice-cold lysis  
157 buffer (20 mM imidazol, 0.25 M NaCl, 1 mM EDTA, in PBS) in the presence of protease  
158 inhibitor cocktail (Roche Applied Science, Indianapolis, IN). The resuspended cells were  
159 sonicated for 1 min on ice (Ultrasonic processor XL; Heat Systems, Farmingdale, NY). The cell  
160 debris was pelleted by centrifugation at 100,000 X g (Beckman 45Ti rotor, 40,000 rpm) for 45

161 min at 4°C, and the protein was purified by a passage over TALON Metal Affinity Resin  
162 (Clontech). Isolated protein was eluted using 200 mM imidazol in PBS. After overnight dialysis  
163 (Slide-A-Lyzer, MWCO 10<sup>4</sup> Daltons, Thermo scientific, Barrington, IL) against filtered PBS, the  
164 final concentration of eGFP-6His was 2 mM. Purified eGFP was stored at -80°C in PBS  
165 containing 20% glycerol.

## 166 **Microscopy**

### 167 *Live cell imaging*

168 The TIRFM and spinning disk confocal microscope systems used in this study have  
169 recently been described in detail (2, 9). The TIRFM system was modified prior to this study to  
170 include a Laser TIRF 3 motorized slider (Carl Zeiss, Inc.; Thornwood, NY), and the spherical  
171 aberration correction unit was removed from the emission path. The penetration depth of the  
172 evanescent field used in these studies was measured using a previously established method (11)  
173 and estimated to be ~150 nm when samples were illuminated with a 488 laser. Slidebook  
174 5.0.0.20 (TIRFM) or 4.2.13 (confocal) imaging software (Intelligent Imaging Innovations, Inc.  
175 (III); Denver, CO) was used to manipulate the hardware devices and visualize data.

176 Cells plated on 25 mm coverslips (No. 1.5, Electron Microscopy Sciences; Hatfield, PA)  
177 16-20 hours prior to imaging were placed into a preheated perfusion chamber on the microscope  
178 stage and overlaid with  $\alpha$ -MEM (no phenol red; Invitrogen) containing 10 mM HEPES pH 7.4  
179 and 5% FBS. The microscope stage and objective lenses were maintained at 37°C within an  
180 environmental chamber, and the air above the cells was supplied with 5% CO<sub>2</sub>.

181 To image CPV- and Tf-TfR interactions on live cells, the virus or protein solution was  
182 cleared of aggregates by centrifugation for 1 min at 14,000 X g in a microfuge, and cells were  
183 inoculated with a dose of material that ensured attachment of <200 objects to the visible cell



184 surface during an imaging period. Tf imaging experiments were performed in the absence of  
185 FBS. Image acquisition was initiated immediately after CPV or Tf addition to cells, and images  
186 were captured at 1-3 s intervals following sequential illumination of the samples with the  
187 appropriate lasers for exposure times of 20-50 ms (confocal) or 10-20 ms (TIRFM). Time-lapse  
188 acquisitions typically spanned 3-4 min per cell in TIRFM experiments and 6-8 min in confocal  
189 experiments.

#### 190 *Fluorescent objects on glass*

191 Fluorescent CPV capsids were nonspecifically adsorbed to glass coverslips to yield ~500  
192 attached particles per field of view. Unbound virus was removed by washing, and single  
193 snapshots were acquired using exposure times equivalent to those in live cell imaging  
194 experiments. Recombinant eGFP molecules were diluted to ~300 nM in PBS and briefly  
195 incubated with a glass coverslip that was modified with a co-polymer of poly-L-lysine (PLL) and  
196 biotinylated polyethylene glycol (PEG) (SuSoS AG; Switzerland) and streptavidin (Sigma-  
197 Aldrich), as previously described (2). Nonspecifically adsorbed molecules were removed by  
198 washing, and bound molecules were photobleached by repeated illumination for 20 ms until a  
199 majority of the molecules no longer fluoresced when excited. The average time to  
200 photobleaching of single eGFP molecules was 40 +/- 38 s (n=576) under these imaging  
201 conditions.

#### 202 **Data analysis**

203 Slidebook 4.2.13 or 5.0.0.18 (III) was used to view and export images, and exported TIFF  
204 files were compiled into AVI Movie files using ImageJ (NIH). SigmaPlot 11.0 (SYSTAT; Point  
205 Richmond, CA) was used to plot data and perform statistical analyses.

#### 206 *Fluorescence intensity measurements*

207 Fluorescence intensity measurements of adaptor proteins and CPV capsids imaged by  
208 confocal microscopy were performed as before (9) using a custom written software application  
209 (IMAB) (28) developed within MATLAB (Mathworks; Natick, MA). In all cases, the local  
210 background signal was subtracted from the pit or capsid signal. IMAB was used to record the  
211 lifetime and peak adaptor signal of the first ~100 coated pits that initiated on the cell surface and  
212 did not capture a CPV capsid. Complete virus uptake events that occurred during the same time  
213 span were analyzed in an identical manner. Coated pits in which adaptor assembly aborted  
214 within 15 s after initiation were excluded from further analysis, as were events in which the  
215 adaptor signal could not be accurately tracked for any portion of the pit lifetime.

216 The fluorescence intensity of eGFP molecules or CPV capsids bound to a glass coverslip  
217 and imaged by TIRFM was measured essentially as described (2) using software developed in  
218 MATLAB. Briefly, the objects were detected as local maxima in an averaged fluorescence image  
219 (average of first 3 frames), and the position of each object was determined by calculating the  
220 mean adjusted center of intensity at each local maximum. A 7 X 7 pixel mask was then centered  
221 on the position of each object, and objects with overlapping masks were eliminated from further  
222 analysis. The fluorescence intensity of the remaining objects was calculated in each image frame  
223 by summing the intensities of the pixels in the 7 X 7 object mask. The object fluorescence  
224 intensity was corrected for local background fluorescence using a routine that 1) generates a  
225 mask to exclude pixels that belong to all objects present in each image plane; 2) computes the  
226 mean and SD of the remaining pixels and excludes the hot pixels (intensity 2.5 SD above the  
227 background mean); 3) sums the first 100 pixels nearest to the center of intensity of the object;  
228 and 4) subtracts the average intensity of those 100 pixels from each pixel within the object mask.  
229 A step-fitting function (2, 20) was employed to identify the time at which each single eGFP

230 molecule photobleached and to measure the fluorescence intensity of each molecule before and  
231 after photobleaching. Photobleaching traces of eGFP molecules were manually sorted to exclude  
232 objects that showed more than one photobleaching step or steps in which the amplitude that was  
233 greater than that of a single molecule.

234 *Analysis of CPV receptor binding, diffusion, dissociation, and entry*

235 The efficiency of clathrin-dependent CPV internalization was measured as follows: (i)  
236 each capsid that arrived in the field but was absent from previous image frame was manually  
237 marked and tracked using Slidebook 5.0.0.18 (Intelligent Imaging Innovations (III); Denver,  
238 CO); (ii) the fate of each particle was tracked until the capsid fluorescence was no longer  
239 detectable above the local background; (iii) particles that were only visible in  $\leq 2$  image frames  
240 (i.e.  $\leq 6$  s) or underwent directed motion (i.e. endosomal particles) were eliminated from further  
241 analysis; (iv) the number of particles that disappeared from view between 2 sequential frames  
242 (i.e. within 3 s) or entered by clathrin-dependent endocytosis was recorded.

243 Events of receptor engagement by CPV capsids were detected and analyzed in the  
244 following manner: (i) all CPV particles that appeared in the field after frame 1 but before frame  
245 90 (2-180 s) of a given time-lapse acquisition were manually identified; (ii) the particle position  
246 in each frame was determined using Slidebook 5.0.0.18 (III) as described below for analysis of  
247 virus diffusion; (iii) the MATLAB software used for analysis of objects on glass was modified to  
248 center a 7 x 7 pixel mask on the virus in each image using the X,Y coordinates of the virus from  
249 Slidebook; (iv) the fluorescence intensity of the virus capsid and associated fTfR-eGFP  
250 molecules were measured in each image frame as for fluorescent objects on glass (see above);  
251 and (v) proper tracking of each virus particle was manually verified, and the fluorescence values  
252 for the virus and fTfR-eGFP were recorded from the frame in which the virus signal was most

253 intense (i.e. the virus was closest to the glass). Frames in which the virus-receptor complex  
254 overlapped with irrelevant spots of receptor fluorescence were not included in the final data set,  
255 and in these cases, the receptor signal associated with the next most intense virus signal was  
256 recorded.

257 Slidebook 5.0.0.18 (III) was used to track the motion of receptor-bound CPV or Tf on the  
258 cell surface. Only objects that arrived in the imaging field after the start of imaging and remained  
259 cell-associated for at least 5 frames were considered for analysis. To map the object position in  
260 each frame, a roughly circular mask comprising 112 pixels was centered on the position of peak  
261 particle fluorescence, and the X, Y coordinates of the mask centroid were recorded. The  
262 measured pixel size ( $0.106 \times 0.106 \mu\text{m}^2$  TIRFM) was used to calculate the object displacement  
263 between frames and the mean squared displacement (MSD) (37) with respect to time. To  
264 calculate the diffusion coefficient (D) of each object, linear regression analysis was performed  
265 using the first 4 time points of a capsid MSD plot to identify the best fit trend line. The formula  
266  $\langle x^2 \rangle = 4Dt$  (37), where  $\langle x^2 \rangle$  is the slope of the best fit line, was used to calculate the D for each  
267 object.

#### 268 **CPV binding, uptake, and infection**

269 To determine the functionality of the eGFP tagged feline TfR, virus binding and uptake  
270 assays were performed in CRFK or TRVb fTfR-eGFP cells as previously described (12). Briefly,  
271 cells were detached from the plate, washed in PBS containing 1% ovalbumin (Sigma-Aldrich),  
272 and incubated in solution with  $10 \mu\text{g/ml}$  of Alexa 647 CPV capsids for the indicated time  
273 intervals at  $37^\circ\text{C}$ . The level of cell-associated capsids was quantified in three independent  
274 experiments for at least 10,000 cells using a FACSCalibur flow cytometer (Becton-Dickinson,  
275 San Jose, CA).

276           The susceptibility of NLFK or TRVb fTfR-eGFP cells to infection with virus was  
277   quantified using previously established methods (31). Cells were inoculated with CPV-2 (MOI  
278   of 5) and incubated at 37°C for 48 h. Cells were fixed with 4% paraformaldehyde in PBS and  
279   then permeabilized with PBS containing 0.1% Triton X-100 and 1% BSA. Permeabilized cells  
280   were immunostained with an Alexa 594-conjugated monoclonal antibody (CE-10) against  
281   nonstructural protein-1 (51).

282

283

284

285

286

287

288

289

290

291

292

293

294

295

296

297

298

299

**RESULTS****300 Visualizing clathrin endocytic structure formation in feline cells**

301 We generated feline kidney CRFK cells that constitutively express an eGFP-tagged  $\sigma 2$   
302 subunit of the AP-2 adaptor complex, a structural constituent of all clathrin endocytic structures  
303 on the plasma membrane (10). As in other mammalian cell types (41), AP-2 localized to the  
304 cytosol and to punctate structures on the plasma membrane of CRFK cells (Figure 1A). Time-  
305 lapse images acquired using a spinning disk confocal microscope revealed that the structures  
306 were dynamic and consisted mostly of diffraction-limited spots that assembled and disappeared  
307 from view with kinetics typical of clathrin-coated pits (Figure 1A, Movie S1) (26, 41). In  
308 addition to the conventional coated pits, CRFK cells formed larger (i.e. not diffraction-limited)  
309 structures that likely correspond to clusters of coated pits and clathrin plaques observed  
310 previously (41, 44), as these structures often accumulated more adaptor proteins and had longer  
311 lifetimes (Figure 1A kymograph). Thus, we isolated feline cells that express a fluorescent  
312 constituent of clathrin endocytic coats, and real-time imaging demonstrated that these cells form  
313 the full array of clathrin endocytic structures observed in other mammalian cell types.

**314 Real-time imaging of clathrin-dependent CPV internalization**

315 We prepared fluorescent CPV capsids by conjugating Alexa Fluor 647 dye molecules to  
316 primary amines exposed on the surface of empty capsids (lacking DNA) using a previously  
317 established procedure that does not interfere with capsid-TfR interactions (16, 19). Structural and  
318 biochemical comparisons of empty and full (DNA-containing) capsids have shown that they are  
319 indistinguishable with regard to the structural elements that control TfR binding (47, 50) and  
320 their dependence on TfR for cell entry (19). Confocal images of the labeled capsids on glass

321 revealed diffraction-limited, fluorescent spots that displayed a single peak distribution of  
322 intensity values, consistent with a population comprised mostly of single capsids (Figure 1B).

323 To visualize CPV internalization by live CRFK  $\sigma$ 2-eGFP cells, we incubated the cells  
324 with fluorescent capsids and acquired images at 3 s intervals using a spinning disk confocal  
325 microscope. Capsids attached to the cell surface and subsequently colocalized with clathrin  
326 endocytic structures containing  $\sigma$ 2-eGFP (Figure 1C, Movie S1). A representative example of  
327 clathrin-dependent CPV internalization is shown in Figure 2 (Movie S2). A capsid attaches to the  
328 cell surface and moves laterally for  $\sim$ 48 s before colliding with an assembling coated pit. The  
329 capsid and coated pit signals remain stably associated after the collision, and the adaptor  
330 fluorescence increases to a maximal value as the coated pit forms around the capsid (Figure 2A,  
331 B). Shortly thereafter, the pit and capsid signals simultaneously disappear, signifying pit  
332 internalization, coat disassembly, and intracellular transport of the capsid-containing vesicle  
333 (Figure 2A, B). This sequence of events is typical of most CPV internalization events and  
334 directly confirms that CPV capsids enter feline cells by the clathrin endocytic pathway.

335 We measured the efficiency of clathrin-dependent CPV internalization by detecting each  
336 capsid binding event and tracking the fate of capsids that remained bound to the cell for at least  
337 two consecutive frames ( $\geq$  6 s). We found that 24% of attached capsids (n=628) entered CRFK  
338 cells by clathrin-dependent endocytosis (Figure 2C), while the majority (76%) of capsids  
339 abruptly disappeared from view before colliding with a coated pit (Figure 2C, D, Movie S3). The  
340 latter capsid disappearance events occurred between consecutive image frames (i.e. in  $<$ 3 s) and  
341 typically less than 30 s after attachment (Figure 2D, E). Under the imaging conditions used here,  
342 photobleaching of the capsid-associated dyes was a gradual process that required at least 250 s  
343 (mean 306  $\pm$  36 s, n=8). Moreover, the field of view was sufficiently deep ( $\sim$ 0.5  $\mu$ m) to

344 visualize the movement of cargo-containing vesicles toward the cell interior before the vesicles  
345 underwent intracellular transport. Thus, capsid disappearance prior to coated pit association was  
346 most probably due to capsid dissociation from TfR on the cell surface and not photobleaching or  
347 endocytic uptake of capsids via a clathrin-independent endocytic mechanism. These data show  
348 that clathrin-dependent endocytosis is the primary pathway of CPV internalization but that most  
349 capsids dissociate from receptors before the CPV-TfR complex encounters an endocytic  
350 structure.

### 351 **CPV diffuses into newly formed clathrin-coated pits**

352 We next analyzed the entry process of capsids captured by forming coated pits in greater  
353 detail. Most capsids (80%; n=347) bound to receptors on the free cell surface and then diffused  
354 laterally into an assembling coated pit (Figure 3A, B). The remainder of capsids either attached  
355 to receptors in or near a forming coated pit (11%) or stopped diffusing at the future site of pit  
356 appearance (9%) (Figure 3A, B). In these infrequent events, we could not resolve whether the  
357 capsids associated with coated pits by diffusion, as the capsid and coat signals were not optically  
358 separable (i.e. they were within ~250 nm of one another) at the time of their initial  
359 colocalization.

360 The elapsed time between CPV attachment and capture by a coated pit (time to capture)  
361 was typically <20 s (Figure 3C). Capsids preferentially associated with coated pits early in the  
362 coat assembly process, as the likelihood of particle incorporation was highest within the first  
363 20% of the coated pit lifetime and lowest after a pit reached 70% of its total lifetime (Figure 3D,  
364 E). Moreover, >90% of stable CPV-coated pit associations (i.e. lasting  $\geq 6$  s) led to capsid  
365 internalization. These results show that CPV-TfR complexes primarily diffuse into newly-  
366 formed coated pits, and that subsequent capsid uptake is highly efficient.



367 **CPV incorporation does not alter the assembly kinetics or clathrin content of coated pits**

368 To assess whether CPV incorporation alters the adaptor composition or assembly kinetics  
369 of clathrin-coated pits in CRFK  $\sigma$ 2-eGFP cells, we measured the maximum AP-2 content (an  
370 indicator of coat size) (10) and the total lifetime of pits that incorporated or lacked a CPV capsid.  
371 We excluded from our analysis the short-lived population of abortive clathrin coats (lifetimes  
372 <15 s) that do not mature into complete coated vesicles, as well as objects that were not  
373 diffraction-limited or could not accurately be tracked over their entire lifetime. Our results show  
374 that CPV incorporation does not alter the lifetime or AP-2 content of clathrin endocytic carriers,  
375 as coated vesicles formed in  $\sim 54 \pm 20$  s (Figure 4A) and had a similar range of peak AP-2  
376 fluorescence values (Figure 4B) regardless of whether they contained a CPV particle.

377 **The entry processes of empty and full CPV capsids are indistinguishable**

378 Next, we directly compared the entry processes of empty and full (DNA-containing) CPV  
379 capsids (summarized in Table 1). We labeled purified full capsids with Atto 647 and imaged  
380 their entry into CRFK  $\sigma$ 2-eGFP cells alone (Table 1, Exp #2) or together with Atto 568 labeled  
381 empty capsids (Table 1, Exp #3). Similar proportions of full and empty capsids entered cells by  
382 clathrin-dependent endocytosis ( $\sim 25\%$ ) or dissociated from receptors on the cell surface before  
383 being captured by a forming coated pit ( $\sim 75\%$ ) (Table 1). Like with empty capsids, a majority of  
384 the full capsids ( $>80\%$ ) diffused laterally into forming coated pits, and full capsid capture by  
385 coated pits preferentially occurred during the early stages of pit formation (Table 1). We  
386 observed modest (2-4 fold) variations in the time to capture of full or empty capsids compared to  
387 the results obtained for empty capsids in earlier experiments (Table 1, Exp #1). However, we  
388 observed these variations for both capsid forms, indicating that the variations did not correlate  
389 with the DNA content of the capsids. The residence time of both capsid forms was also longer in

390 Exp #2 and #3 compared to that of the empty capsids analyzed in Exp #1, but this difference was  
391 also relatively minor (<2-fold). From these data, we conclude that that full and empty CPV  
392 capsids access clathrin endocytic structures in the same way, a result that is consistent with the  
393 high degree of structural similarity between the two capsid forms (47, 50).

#### 394 **Receptor-bound CPV capsids diffuse slower than single TfRs**

395 To address whether CPV binding alters the rate of TfR diffusion, we used Total Internal  
396 Reflection Fluorescence Microscopy (TIRFM) to image CPV diffusion prior to coated pit  
397 association and compared the rate of capsid diffusion with that of individual TfRs. In these  
398 experiments, we inoculated cells with low doses of capsids or Atto 647-labeled Tf molecules (to  
399 label single TfR dimers) to allow unambiguous particle tracking. As observed by confocal  
400 microscopy, capsids explored large areas of the plasma membrane before encountering and being  
401 internalized by coated pits (Figure 5A-C, Movie S4). In some cases, capsids became transiently  
402 confined to submicron sized areas of the plasma membrane (Figure 5C), as previously seen for  
403 individual TfRs (43). Plots of the mean squared displacement (MSD) of the capsids were nearly  
404 always linear with respect to time during the early stages of virus diffusion, consistent with a  
405 random walk mechanism of two-dimensional diffusion (Figure 5D). Using the MSD plots, we  
406 calculated the macroscopic diffusion coefficient (D) for 104 individual CPV capsids and  
407 obtained a mean value of  $0.014 \mu\text{m}^2 \text{s}^{-1}$  (Figure 5E). In contrast, Atto 647-labeled Tf molecules  
408 bound to single TfRs had a mean D value of  $0.15 \mu\text{m}^2 \text{s}^{-1}$  (Figure 5E, Movie S5), consistent with  
409 previous reports (43). Thus, CPV-TfR complexes diffused slower than Tf-TfR complexes.

#### 410 **CPV capsids cluster TfRs on the cell surface**

411 To directly visualize CPV-TfR interactions on the surface of live cells, we appended  
412 eGFP or mCherry to the C-terminal ectodomain of the wt feline TfR (fTfR) (Figure 6A). We

413 then stably expressed the tagged receptors in Chinese hamster ovary TRVb cells, which lack  
414 endogenous TfRs and therefore do not support CPV attachment, entry, or infection (29, 33). CPV  
415 bound and entered TRVb cells expressing the tagged receptors with similar kinetics to those  
416 observed in CRFK cells, and capsids accumulated together with receptors in endosomal  
417 compartments (Figure 6B, C). In TRVb cells co-expressing  $\sigma 2$ -eGFP and fTfR-mCherry, we  
418 observed the binding, diffusion, and clathrin-dependent uptake of capsids (Figure S1A-D, Movie  
419 S6). The kinetics of capsid diffusion and capture, as well as the efficiency of capture and  
420 internalization, were indistinguishable from those observed in CRFK cells (Table 1, Exp #4).  
421 Moreover, fTfR-mCherry or fTfR-eGFP supported productive cell infection by CPV (data not  
422 shown), indicating that the fluorescent molecules did not prevent a downstream TfR-dependent  
423 step of virus entry. The tagged receptors also bound and internalized Tf, albeit less efficiently  
424 than wt TfRs (Figure S1E). These data show that the fTfR fusion proteins support efficient CPV  
425 entry and infection in TRVb cells.

426         The intensity of the evanescent wave generated under TIR conditions decreases  
427 exponentially with increasing distance from the glass coverslip (Figure 6D). Thus, prior to  
428 imaging CPV-TfR interactions on the cell surface, we measured the fluorescent signals of single  
429 eGFP molecules and CPV capsids bound to a coverslip to establish the maximum possible  
430 fluorescence intensity of the objects. Single eGFP molecules showed a normal distribution of  
431 fluorescence intensities centered at  $3082 \pm 661$  arbitrary fluorescence units (a.u.) (Figure S2A-  
432 C), while the intensities of Atto 647-labeled capsids distributed across a broader range ( $16911 \pm$   
433  $7906$  a.u.) that was equivalent to the fluorescence of one to eight Atto 647 dye molecules (Figure  
434 S2D-F).

435           Next we examined whether CPV capsids cluster receptors on the cell surface. We  
436 inoculated the cells with Atto 647 capsids as before and acquired images at 2 s intervals by  
437 TIRFM. We then detected events in which a capsid appeared in the field of view <3 min after the  
438 onset of imaging, a time at which most particles are still on the cell surface. An example of such  
439 an event is shown in Figure 6E (Movie S7). A capsid appears in the field of view and colocalizes  
440 with a spot of receptor that remains visible as the particle diffuses laterally on the cell surface.  
441 Importantly, the fluorescence intensities of the capsid and receptors varied together as a function  
442 of time, reflecting changes in the Z position of the capsid, as expected if the capsid was bound to  
443 a defined set of TfR-eGFP molecules (Figure 6E; see Figure S3 for additional examples).

444           For 76 such events, we recorded the virus and receptor fluorescence values from the  
445 image frame in which the virus signal was most intense (i.e. when the CPV-TfR complex was  
446 closest to the glass) (Figure 6E). The median signal of the cell-associated capsids imaged by  
447 TIRFM was 3.5-fold lower than that of capsids directly attached to the glass coverslip (Figure  
448 6F). This result indicates that the CPV-TfR complexes were close (<400 nm) but not in direct  
449 contact with the coverslip and were therefore illuminated by a less intense portion of the  
450 evanescent field (Figure 6D). The eGFP fluorescence signal of most complexes (55/76) was  
451  $\leq 12,000$  arbitrary fluorescence units (Figure 6F), which corresponded to  $\leq 4$  eGFP molecules, or  
452  $\leq 2$  receptor dimers. After correction for the positional offset of the complexes from the coverslip  
453 by a factor of 3.5, we determined that most capsids bound fewer than 5 receptors with an upper  
454 limit of 8 receptors per capsid (Figure 6F). We also observed a second class of objects in which  
455 the capsids colocalized with receptor spots of 2-3 fold higher intensity. In these cases, the capsid  
456 motion was often restricted or directed (Figure S3C), suggesting that the particles were in a

457 coated pit or an endocytic vesicle. We conclude that most CPV capsids cluster fewer than 5 fTfR

458 dimers on the surface of live feline cells.

459

460

461

462

463

464

465

466

467

468

469

470

471

472

473

474

475

476

477

478

479

480

**DISCUSSION**

481 We investigated how receptor binding by a small non-enveloped virus, canine parvovirus  
482 (CPV), governs virus capsid uptake by clathrin endocytic structures. By visualizing the initial  
483 entry stages of individual capsids bound to TfR molecules, we resolved previously unappreciated  
484 aspects of capsid entry that support the following conclusions: (i) capsids clustered up to eight  
485 TfRs on the cell surface; (ii) ~25% of attached capsids entered feline cells by clathrin-dependent  
486 endocytosis, while the remainder dissociated from receptors before engaging a clathrin-coated  
487 pit; and (iii) capsids engaged the clathrin system by diffusing into assembling coated pits. Based  
488 on these conclusions, we propose a model whereby TfRs tether CPV to target cells, and limited  
489 TfR clustering increases the probability of capsid association with a coated pit by allowing long-  
490 range diffusion of the CPV-TfR complex and by increasing the residence time of capsids on the  
491 cell surface (Figure 7).

492 CPV capsids bound to TfRs entered feline cells by clathrin-dependent endocytosis. We  
493 did not observe evidence for clathrin-independent uptake of CPV. Instead, capsids that did not  
494 associate with a coated pit suddenly dissociated from receptors on the cell surface. Our results  
495 are consistent with previous electron microscopic images of CPV in coated pits but not other  
496 endocytic structures (34) and with the known clathrin-dependent uptake mechanism of TfRs (3).  
497 Thus, we have directly confirmed that CPV enters feline cells by clathrin-dependent endocytosis  
498 and further show that in this cell culture system where capsids are not confined to the cell surface  
499 by adjacent cells, most capsids dissociate from feline TfRs prior to encountering a clathrin  
500 endocytic structure.

501 The half-life of CPV-TfR complexes calculated from the capsid residence times on  
502 CRFK cells was ~30 s, which is ~15-fold shorter than that of holotransferrin-TfR complexes (~8

503 min) on other mammalian cells (17, 49). The short half-life of CPV-TfR complexes indicates that  
504 CPV has a much lower affinity for TfR than holotransferrin ( $K_d \sim 5$  nM) (24, 49). We speculate  
505 that this low receptor affinity, combined with steric limitations imposed by the capsid  
506 architecture, restricts the number of receptors that simultaneously engage a capsid. In turn, this  
507 limited receptor clustering allows the CPV-TfR complex to laterally diffuse over large areas of  
508 the cell surface, thereby increasing the probability of capsid collision with an assembling coated  
509 pit. Whether capsid dissociation from TfRs is also required for intracellular steps of virus entry  
510 (e.g. endosomal membrane penetration) remains to be determined. Since CPV and the related  
511 parvovirus, feline panleukopenia virus (FPV), differ in their affinities for the feline and canine  
512 TfRs (18), it is of interest to explore how these differences in receptor affinity influence the virus  
513 entry process.

514 CPV capsids diffused into coated pits that had already initiated on the cell surface. This  
515 mode of cargo capture is similar to that of low density lipoprotein (LDL)-receptor complexes  
516 (10) and to that of dengue virus serotype 2 (DENV) (48) but apparently distinct from that of  
517 vesicular stomatitis virus (VSV) and influenza A virus (8, 40). These latter viruses do not diffuse  
518 over large areas of the plasma membrane or engage existing coated pits. Instead, they incorporate  
519 into pits that initiate near or beneath the site of virus attachment (8, 40). These differences in  
520 virus mobility and capture mode correlate with the receptor binding capacity of the virus  
521 particles, as VSV and influenza A virus are larger and contain more receptor binding proteins  
522 than DENV or CPV. The fact that nearly all CPV capsids diffused into coated pits that had  
523 already initiated on the cell surface also shows that the low level of TfR clustering by CPV does  
524 not induce coated pit formation beneath attached capsids. Our results contrast with recent  
525 evidence suggesting that clustering of biotinylated TfRs (bTfRs) by tetravalent streptavidin

526 complexes (SA) promotes coated pit initiation (25). Unlike our findings with CPV-TfR  
527 complexes, bTfR-SA complexes are presumably stable due to the high affinity of SA for biotin  
528 ( $K_d \sim 10^{-14}$  M) (13). Perhaps these or other properties of the ligand-receptor complexes influence  
529 whether they can serve as scaffolds for coated pit initiation.

530 CPV engaged coated pits faster than all other viruses studied to date. Most capsids  
531 associated with coated pits less than 20 s after receptor binding, while the average time to  
532 capture for DENV, influenza A virus, and VSV ranged from 20 s to several minutes (8, 40, 48).  
533 That coated pit assembly around these viruses typically requires at least 30 s indicates that the  
534 coat assembly process is the rate-limiting step for CPV uptake, while the time required for virus  
535 capture is often rate-limiting for the other viruses. Although CPV capture was rapid, only 25% of  
536 attached capsids encountered a coated pit before dissociating from the cell surface. In contrast,  
537 approximately 65% of influenza A viruses and 90% of VSV particles associated with coated pits  
538 after attachment (8, 40). In the case of VSV, attached virions did not dissociate from receptors on  
539 the cell surface (8), suggesting that the stability of VSV-receptor complexes translates into a  
540 higher probability of capture by a coated pit compared to CPV.

541 The potential importance of receptor clustering for virus entry has been inferred from the  
542 multivalent character of the particles themselves, but only the clustering of DC-SIGN by  
543 Uukuniemi virus has been directly visualized on the cell surface (27). Here we show that most  
544 CPV capsids cluster fewer than 5 TfRs on the plasma membrane of live feline cells. This finding  
545 is consistent with the presence of multiple receptor binding sites on one hemisphere of the capsid  
546 surface and with *in vitro* biochemical measurements showing that capsids in solution bind up to  
547 7 TfR ectodomains (14). By comparing the diffusion rates of CPV and Tf bound to untagged  
548 TfRs, we found that CPV binding reduced the rate of TfR diffusion in the plasma membrane. We



549 propose that the slower diffusion of the CPV-TfR complexes results from transient stages of  
550 receptor clustering by capsids that either reduce the free diffusion rate of the complexes or the  
551 rate at which the complexes migrate between submicron-sized compartments of membrane  
552 delimited by the underlying cell cytoskeleton (42). Indeed, previous studies showed that  
553 increasing the density of GM1 ganglioside receptors in an artificial membrane reduced the  
554 diffusion rate of simian virus 40 particles by inducing transient stages of virus confinement (22).

555         In summary, our data directly show that CPV-TfR interactions transport viral capsids into  
556 assembling clathrin endocytic structures by a relatively rapid diffusion-based mechanism. Given  
557 that CPV engages a low number of TfRs, this mechanism of cargo incorporation likely also  
558 extends to free and Tf-bound TfRs and as well as other viruses that might exploit the natural  
559 endocytic function of non-signaling receptors to engage endocytic structures. Notably, TfRs also  
560 function as receptors for other viral pathogens, including mouse mammary tumor virus and  
561 certain New World arenaviruses (38, 39). These virus particles are significantly larger and have a  
562 greater receptor binding capacity than CPV. Thus, we anticipate that comparative analyses of  
563 these virus-receptor systems will reveal differences in the properties of virus-receptor complexes  
564 that modulate cargo capture by clathrin endocytic structures.

565

566

## ACKNOWLEDGEMENTS

567

We gratefully acknowledge Wendy Weichert for expert technical assistance and Ramiro

568

Massol for the development of the IMAB image analysis software. We also thank Eric Marino

569

for maintaining the confocal and TIRF microscope systems used in this study.

570

571

572

573

574

575

576

577

578

579

580

581

582

583

584

585

586

587

588

589

## REFERENCES

- 590 1. **Agbandje, M., R. McKenna, M. G. Rossmann, M. L. Strassheim, and C. R. Parrish.**  
591 1993. Structure determination of feline panleukopenia virus empty particles. *Proteins*  
592 **16**:155-71.
- 593 2. **Bocking, T., F. Aguet, S. C. Harrison, and T. Kirchhausen.** 2011. Single-molecule  
594 analysis of a molecular disassemblase reveals the mechanism of Hsc70-driven clathrin  
595 uncoating. *Nat Struct Mol Biol* **18**:295-301.
- 596 3. **Booth, A. G., and M. J. Wilson.** 1981. Human placental coated vesicles contain  
597 receptor-bound transferrin. *Biochem J* **196**:355-62.
- 598 4. **Cheng, Y., O. Zak, P. Aisen, S. C. Harrison, and T. Walz.** 2004. Structure of the  
599 human transferrin receptor-transferrin complex. *Cell* **116**:565-76.
- 600 5. **Collawn, J. F., A. Lai, D. Domingo, M. Fitch, S. Hatton, and I. S. Trowbridge.** 1993.  
601 YTRF is the conserved internalization signal of the transferrin receptor, and a second  
602 YTRF signal at position 31-34 enhances endocytosis. *J Biol Chem* **268**:21686-92.
- 603 6. **Conner, S. D., and S. L. Schmid.** 2003. Regulated portals of entry into the cell. *Nature*  
604 **422**:37-44.
- 605 7. **Crandell, R. A., C. G. Fabricant, and W. A. Nelson-Rees.** 1973. Development,  
606 characterization, and viral susceptibility of a feline (*Felis catus*) renal cell line (CRFK).  
607 *In Vitro* **9**:176-85.
- 608 8. **Cureton, D. K., R. H. Massol, S. Saffarian, T. L. Kirchhausen, and S. P. Whelan.**  
609 2009. Vesicular stomatitis virus enters cells through vesicles incompletely coated with  
610 clathrin that depend upon actin for internalization. *PLoS Pathog* **5**:e1000394.

- 611 9. **Cureton, D. K., R. H. Massol, S. P. Whelan, and T. Kirchhausen.** 2010. The length of  
612 vesicular stomatitis virus particles dictates a need for actin assembly during clathrin-  
613 dependent endocytosis. *PLoS Pathog* **6**.
- 614 10. **Ehrlich, M., W. Boll, A. Van Oijen, R. Hariharan, K. Chandran, M. L. Nibert, and**  
615 **T. Kirchhausen.** 2004. Endocytosis by random initiation and stabilization of clathrin-  
616 coated pits. *Cell* **118**:591-605.
- 617 11. **Gell, C., M. Berndt, J. Enderlein, and S. Diez.** 2009. TIRF microscopy evanescent  
618 field calibration using tilted fluorescent microtubules. *J Microsc* **234**:38-46.
- 619 12. **Goodman, L. B., S. M. Lyi, N. C. Johnson, J. O. Cifuentes, S. L. Hafenstein, and C.**  
620 **R. Parrish.** 2010. Binding site on the transferrin receptor for the parvovirus capsid and  
621 effects of altered affinity on cell uptake and infection. *J Virol* **84**:4969-78.
- 622 13. **Green, N. M.** 1975. Avidin. *Adv Protein Chem* **29**:85-133.
- 623 14. **Hafenstein, S., L. M. Palermo, V. A. Kostyuchenko, C. Xiao, M. C. Morais, C. D.**  
624 **Nelson, V. D. Bowman, A. J. Battisti, P. R. Chipman, C. R. Parrish, and M. G.**  
625 **Rossmann.** 2007. Asymmetric binding of transferrin receptor to parvovirus capsids. *Proc*  
626 *Natl Acad Sci U S A* **104**:6585-9.
- 627 15. **Harbison, C. E., J. A. Chiorini, and C. R. Parrish.** 2008. The parvovirus capsid  
628 odyssey: from the cell surface to the nucleus. *Trends Microbiol* **16**:208-14.
- 629 16. **Harbison, C. E., S. M. Lyi, W. S. Weichert, and C. R. Parrish.** 2009. Early steps in  
630 cell infection by parvoviruses: host-specific differences in cell receptor binding but  
631 similar endosomal trafficking. *J Virol* **83**:10504-14.

- 632 17. **Harding, C., J. Heuser, and P. Stahl.** 1983. Receptor-mediated endocytosis of  
633 transferrin and recycling of the transferrin receptor in rat reticulocytes. *J Cell Biol*  
634 **97**:329-39.
- 635 18. **Hueffer, K., L. Govindasamy, M. Agbandje-McKenna, and C. R. Parrish.** 2003.  
636 Combinations of two capsid regions controlling canine host range determine canine  
637 transferrin receptor binding by canine and feline parvoviruses. *J Virol* **77**:10099-105.
- 638 19. **Hueffer, K., J. S. Parker, W. S. Weichert, R. E. Geisel, J. Y. Sgro, and C. R. Parrish.**  
639 2003. The natural host range shift and subsequent evolution of canine parvovirus resulted  
640 from virus-specific binding to the canine transferrin receptor. *J Virol* **77**:1718-26.
- 641 20. **Kerssemakers, J. W., E. L. Munteanu, L. Laan, T. L. Noetzel, M. E. Janson, and M.**  
642 **Dogterom.** 2006. Assembly dynamics of microtubules at molecular resolution. *Nature*  
643 **442**:709-12.
- 644 21. **Kirchhausen, T.** 2009. Imaging endocytic clathrin structures in living cells. *Trends Cell*  
645 *Biol* **19**:596-605.
- 646 22. **Kukura, P., H. Ewers, C. Muller, A. Renn, A. Helenius, and V. Sandoghdar.** 2009.  
647 High-speed nanoscopic tracking of the position and orientation of a single virus. *Nat*  
648 *Methods* **6**:923-7.
- 649 23. **Lawrence, C. M., S. Ray, M. Babyonyshev, R. Galluser, D. W. Borhani, and S. C.**  
650 **Harrison.** 1999. Crystal structure of the ectodomain of human transferrin receptor.  
651 *Science* **286**:779-82.
- 652 24. **Lebron, J. A., A. P. West, Jr., and P. J. Bjorkman.** 1999. The hemochromatosis  
653 protein HFE competes with transferrin for binding to the transferrin receptor. *J Mol Biol*  
654 **294**:239-45.

- 655 25. **Liu, A. P., F. Aguet, G. Danuser, and S. L. Schmid.** 2011. Local clustering of  
 656 transferrin receptors promotes clathrin-coated pit initiation. *J Cell Biol* **191**:1381-93.
- 657 26. **Loerke, D., M. Mettlen, D. Yarar, K. Jaqaman, H. Jaqaman, G. Danuser, and S. L.**  
 658 **Schmid.** 2009. Cargo and dynamin regulate clathrin-coated pit maturation. *PLoS Biol*  
 659 **7**:e57.
- 660 27. **Lozach, P. Y., A. Kuhbacher, R. Meier, R. Mancini, D. Bitto, M. Bouloy, and A.**  
 661 **Helenius.** 2011. DC-SIGN as a Receptor for Phleboviruses. *Cell Host Microbe* **10**:75-88.
- 662 28. **Massol, R. H., W. Boll, A. M. Griffin, and T. Kirchhausen.** 2006. A burst of auxilin  
 663 recruitment determines the onset of clathrin-coated vesicle uncoating. *Proc Natl Acad Sci*  
 664 *U S A* **103**:10265-70.
- 665 29. **McGraw, T. E., L. Greenfield, and F. R. Maxfield.** 1987. Functional expression of the  
 666 human transferrin receptor cDNA in Chinese hamster ovary cells deficient in endogenous  
 667 transferrin receptor. *J Cell Biol* **105**:207-14.
- 668 30. **Mercer, J., M. Schelhaas, and A. Helenius.** 2010. Virus entry by endocytosis. *Annu*  
 669 *Rev Biochem* **79**:803-33.
- 670 31. **Palermo, L. M., S. L. Hafenstein, and C. R. Parrish.** 2006. Purified feline and canine  
 671 transferrin receptors reveal complex interactions with the capsids of canine and feline  
 672 parvoviruses that correspond to their host ranges. *J Virol* **80**:8482-92.
- 673 32. **Palermo, L. M., K. Hueffer, and C. R. Parrish.** 2003. Residues in the apical domain of  
 674 the feline and canine transferrin receptors control host-specific binding and cell infection  
 675 of canine and feline parvoviruses. *J Virol* **77**:8915-23.

- 676 33. **Parker, J. S., W. J. Murphy, D. Wang, S. J. O'Brien, and C. R. Parrish.** 2001.  
 677 Canine and feline parvoviruses can use human or feline transferrin receptors to bind,  
 678 enter, and infect cells. *J Virol* **75**:3896-902.
- 679 34. **Parker, J. S., and C. R. Parrish.** 2000. Cellular uptake and infection by canine  
 680 parvovirus involves rapid dynamin-regulated clathrin-mediated endocytosis, followed by  
 681 slower intracellular trafficking. *J Virol* **74**:1919-30.
- 682 35. **Parrish, C. R.** 1991. Mapping specific functions in the capsid structure of canine  
 683 parvovirus and feline panleukopenia virus using infectious plasmid clones. *Virology*  
 684 **183**:195-205.
- 685 36. **Parrish, C. R., and Y. Kawaoka.** 2005. The origins of new pandemic viruses: the  
 686 acquisition of new host ranges by canine parvovirus and influenza A viruses. *Annu Rev*  
 687 *Microbiol* **59**:553-86.
- 688 37. **Qian, H., M. P. Sheetz, and E. L. Elson.** 1991. Single particle tracking. Analysis of  
 689 diffusion and flow in two-dimensional systems. *Biophys J* **60**:910-21.
- 690 38. **Radoshitzky, S. R., J. Abraham, C. F. Spiropoulou, J. H. Kuhn, D. Nguyen, W. Li,**  
 691 **J. Nagel, P. J. Schmidt, J. H. Nunberg, N. C. Andrews, M. Farzan, and H. Choe.**  
 692 2007. Transferrin receptor 1 is a cellular receptor for New World haemorrhagic fever  
 693 arenaviruses. *Nature* **446**:92-6.
- 694 39. **Ross, S. R., J. J. Schofield, C. J. Farr, and M. Bucan.** 2002. Mouse transferrin receptor  
 695 1 is the cell entry receptor for mouse mammary tumor virus. *Proc Natl Acad Sci U S A*  
 696 **99**:12386-90.

- 697 40. **Rust, M. J., M. Lakadamyali, F. Zhang, and X. Zhuang.** 2004. Assembly of endocytic  
698 machinery around individual influenza viruses during viral entry. *Nat Struct Mol Biol*  
699 **11**:567-73.
- 700 41. **Saffarian, S., E. Cocucci, and T. Kirchhausen.** 2009. Distinct dynamics of endocytic  
701 clathrin-coated pits and coated plaques. *PLoS Biol* **7**:e1000191.
- 702 42. **Sako, Y., and A. Kusumi.** 1995. Barriers for lateral diffusion of transferrin receptor in  
703 the plasma membrane as characterized by receptor dragging by laser tweezers: fence  
704 versus tether. *J Cell Biol* **129**:1559-74.
- 705 43. **Sako, Y., and A. Kusumi.** 1994. Compartmentalized structure of the plasma membrane  
706 for receptor movements as revealed by a nanometer-level motion analysis. *J Cell Biol*  
707 **125**:1251-64.
- 708 44. **Taylor, M. J., D. Perrais, and C. J. Merrifield.** 2011. A high precision survey of the  
709 molecular dynamics of mammalian clathrin-mediated endocytosis. *PLoS Biol*  
710 **9**:e1000604.
- 711 45. **Traub, L. M.** 2009. Tickets to ride: selecting cargo for clathrin-regulated internalization.  
712 *Nat Rev Mol Cell Biol* **10**:583-96.
- 713 46. **Trowbridge, I. S., and M. B. Omary.** 1981. Human cell surface glycoprotein related to  
714 cell proliferation is the receptor for transferrin. *Proc Natl Acad Sci U S A* **78**:3039-43.
- 715 47. **Tsao, J., M. S. Chapman, M. Agbandje, W. Keller, K. Smith, H. Wu, M. Luo, T. J.**  
716 **Smith, M. G. Rossmann, R. W. Compans, and et al.** 1991. The three-dimensional  
717 structure of canine parvovirus and its functional implications. *Science* **251**:1456-64.



718 48. **van der Schaar, H. M., M. J. Rust, C. Chen, H. van der Ende-Metselaar, J.**  
719 **Wilschut, X. Zhuang, and J. M. Smit.** 2008. Dissecting the cell entry pathway of  
720 dengue virus by single-particle tracking in living cells. *PLoS Pathog* **4**:e1000244.

721 49. **Ward, J. H., J. P. Kushner, and J. Kaplan.** 1982. Transferrin receptors of human  
722 fibroblasts. Analysis of receptor properties and regulation. *Biochem J* **208**:19-26.

723 50. **Wu, H., and M. G. Rossmann.** 1993. The canine parvovirus empty capsid structure. *J*  
724 *Mol Biol* **233**:231-44.

725 51. **Yeung, D. E., G. W. Brown, P. Tam, R. H. Russnak, G. Wilson, I. Clark-Lewis, and**  
726 **C. R. Astell.** 1991. Monoclonal antibodies to the major nonstructural nuclear protein of  
727 minute virus of mice. *Virology* **181**:35-45.

728

729

730

731

732

733

734

735

736

737

738

739

740

741

**FIGURE LEGENDS****742 Figure 1. CPV association with clathrin endocytic structures in feline cells.**

743 (A) Clathrin-coated vesicle formation in CRFK cells. Left, image of a CRFK  $\sigma$ 2-eGFP cell  
744 extracted from frame 1 of a 10 min time-lapse acquisition. Images were captured at 3 s intervals  
745 using a spinning disk confocal microscope. Right, kymograph view of clathrin-coated vesicle  
746 formation by the cell shown at left.

747 (B) Fluorescence intensity of Alexa 647 CPV capsids. Confocal images of labeled capsids on  
748 glass were acquired, and the fluorescence intensity of each capsid spot was quantified. Inset,  
749 enlarged view of capsids (red) on glass.

750 (C) Colocalization of CPV capsids with clathrin-coated pits (Movie S1). CRFK  $\sigma$ 2-eGFP cells  
751 were inoculated with Alexa 647 capsids and imaged as in A. A merge of the AP-2 (green) and  
752 capsid (red) channels is shown, along with an enlarged view of 2 capsids in coated pits from the  
753 boxed region at left. Arrowheads highlight capsids in (yellow) or outside (red) coated pits.

**754 Figure 2. Real-time imaging of clathrin-dependent CPV internalization.**

755 (A) Example of clathrin-dependent CPV endocytosis (Movie S2). Left panels, CRFK  $\sigma$ 2-eGFP  
756 cells (green, AP-2) were inoculated with fluorescent capsids (red) and imaged as before. The  
757 image frame prior to capsid attachment was set to  $t=0$  s. The capsid attaches in frame +3 and  
758 diffuses laterally on the cell surface. The coated pit that is the future site of capsid uptake  
759 initiates in frame +33 while the capsid is still undergoing diffusion. The capsid collides with the  
760 assembling pit in frame +51, and the capsid and pit signals remain colocalized, signifying capsid  
761 incorporation into the pit. Frame +87 depicts the capsid-containing pit during the process of  
762 internalization (note the decrease in the capsid and AP-2 fluorescence). Right panel, diffusion

763 path of the capsid shown at left. A color-coded line trace of the capsid diffusion path is overlaid  
764 onto the  $t=51$  s image.

765 (B) Plot of the background corrected AP-2 (green) and capsid (red) fluorescence intensities with  
766 respect to time for the event in A. For frames prior to pit initiation, the AP-2 fluorescence  
767 intensity was quantified at the eventual site pit initiation.

768 (C) Efficiency of clathrin-dependent CPV entry. Efficiency is expressed as a percentage of the  
769 total particles that bound to cells during time-lapse imaging of 4 cells. The percentage of  
770 particles that entered by clathrin-dependent endocytosis was 8% (9 enter/108 total), 30%  
771 (38/125), 24% (52/220), and 27% (48/175).

772 (D) Examples of CPV dissociation from the cell surface (Movie S3). Time-lapse images showing  
773 the attachment (downward facing arrows) of two capsids (red; #1, #2) and subsequent capsid  
774 dissociation (upward facing arrows).

775 (E) Residence time of CPV capsids that dissociated from CRFK cells. The elapsed time between  
776 capsid attachment and disappearance was measured for capsids that remained bound for  $\geq 6$  s.  
777 Events are from the same 4 cells that were analyzed in C.

778 **Figure 3. CPV capsids diffuse into newly-formed clathrin-coated pits.**

779 (A) Schematics depicting how CPV capsids incorporate into coated pits. For each clathrin-  
780 dependent CPV entry event, the process of capsid-pit association was analyzed and recorded.  
781 The events were assigned to one of the four observed categories (numbered 1-4).

782 (B) Chart showing the frequency of each capture mode. Data are from 18 cells. The data set(s)  
783 that comprise each slice are indicated according to the nomenclature in A.

784 (C) The time interval between particle attachment and capture by a coated pit. The mean time to  
785 capture was  $12 \pm 14$  s.

786 (D and E) Timing of CPV capture expressed relative to the time of coated pit initiation (D) or as  
787 a percentage of the total pit lifetime (E). In E, 0% = pit initiation, 100% = loss of adaptor signal.

788 **Figure 4. CPV does not alter the assembly kinetics or adaptor content of coated pits.**

789 Confocal images of CRFK  $\sigma$ 2-eGFP cells were acquired at 3 s intervals.

790 (A) Total lifetime of conventional coated pits (left) or pits that internalized a CPV capsid (right).

791 Data for standard coated pits are from 4 individual cells in the presence of CPV, and data for

792 CPV-containing pits are from 17 cells and include events from data sets #1 and #2 (Figure 3A).

793 The average lifetime of standard coated pits ( $54 \pm 19$  s) and CPV-containing pits ( $53 \pm 19$  s) is

794 not significantly different (Two-tailed Student's t-test,  $P=0.33$ ).

795 (B) Lifetime versus maximum AP-2 fluorescence of standard (left) or CPV-containing (right)

796 coated pits. Data for standard coated pits are from 4 cells. CPV data are from the same 4 cells

797 and include events in data sets #1 and #2. Each open circle represents a single coated pit. The

798 average peak fluorescence of AP-2 in standard coated pits ( $43 \pm 1.8 \times 10^3$ ) and CPV-containing

799 pits ( $45 \pm 2.0 \times 10^3$ ) is not significantly different (Two-tailed Student's t-test,  $P=0.44$ ).

800 **Figure 5. Receptor-bound CPV capsids diffuse slower than single TfRs.**

801 (A) CPV diffusion and uptake imaged by TIRFM. CRFK  $\sigma$ 2-eGFP cells were inoculated with

802 fluorescent CPV capsids, and images were captured at 1 s intervals. Left, frame 194 of a 5 min

803 time-lapse acquisition showing capsids (red) present on the free cell surface (red arrowheads) or

804 colocalizing with AP-2 (green) in coated pits (yellow or blue arrowheads). Inset shows a zoomed

805 view of two capsids in coated pits from the boxed region below. Right, kymograph view of

806 coated pit formation over time in the cell shown at left. The blue arrowhead highlights

807 internalization of the same capsid marked with a blue arrowhead at left. A zoomed view of the

808 event is provided below.

809 (B) Example CPV internalization event observed by TIRFM (Movie S4). Frames prior to virus  
 810 capture are spaced at 1 s intervals, and frames after virus capture are spaced at 3 s intervals.  
 811 Scale bar, 1  $\mu$ m.

812 (C) Example traces of capsid diffusion. Traces of four capsids are displayed in separate colors.  
 813 The start of each trace is centered at (X=0, Y=0). Small points indicate the particle position in  
 814 sequential frames spaced at 1 s intervals. Large dots indicate the location of particle capture by a  
 815 coated pit. The light blue trace corresponds to the diffusion path of the capsid highlighted by a  
 816 blue arrowhead in A and B.

817 (D) Mean square displacement plots for the objects shown in C. The diffusion coefficient (D) for  
 818 each capsid is provided. Plot colors refer to traces of the same color in panel C.

819 (E) Diffusion coefficients of receptor-bound Tf (gray, Movie S5) or CPV (red). Gray bars  
 820 designate the mean of each population. Tf and CPV data are from 6 and 8 cells, respectively.

821 **Figure 6. CPV capsids cross-link TfRs on the cell surface of live cells.**

822 (A) Schematics of fTfR tagged with eGFP. The eGFP molecule was appended to the C-terminal  
 823 ectodomain of the fTfR such that each receptor dimer contains two eGFPs.

824 (B) Images of CPV capsids colocalizing with fTfR-eGFP in endosomal compartments. TRVb  
 825 cells stably expressing fTfR-eGFP (green) were inoculated with Atto 647 CPV capsids (red) and  
 826 incubated at 37°C for 10 min. Live cells were imaged by TIRFM, and a representative image  
 827 from a time-lapse acquisition is shown. Right-hand panels show an expanded view of the boxed  
 828 region at left. The fTfR-eGFP channel is shown as a merge with the Atto 647 CPV channel (top)  
 829 or alone (bottom). Arrowheads highlight the receptor signal in endosomes that contain CPV.  
 830 Scale bar in right panels, 1  $\mu$ m.

831 (C) Comparison of CPV binding and uptake in CRFK or TRVb fTfR-eGFP cells. Cells were  
832 inoculated with Alexa 647 CPV capsids at  $t=0$  and  $37^{\circ}\text{C}$ , and the cell-associated capsid  
833 fluorescence was quantified by flow cytometry at the indicated times for the receptor-expressing  
834 cells. At all times, 2-5 fold more capsids associated with TRVb fTfR-eGFP cells than with  
835 CRFK cells. To compare the rates of capsid association with both cells types, we expressed the  
836 raw fluorescence values as a fraction of the values obtained at 20 min p.i. in each cell type. Data  
837 points are the mean  $\pm$  SD of 3 experiments. Asterisks indicate time points when the difference in  
838 the mean values is statistically significant (Two-tailed Student's t-test,  $P<0.05$ ).

839 (D) Schematic illustrating the position dependence of CPV-fTfR-eGFP complex detection using  
840 TIRFM. The intensity of the evanescent wave (gray) generated from the totally internally  
841 reflected laser source decreases exponentially as the distance from the coverslip increases. Thus,  
842 CPV capsids (red) and the associated fTfR-eGFP molecules (green) are maximally excited when  
843 directly contacting the glass coverslip, but those on the upper cell surface are excited to a lesser  
844 extent and therefore emit a lower fluorescent signal.

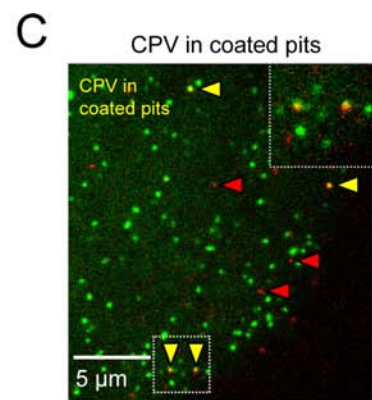
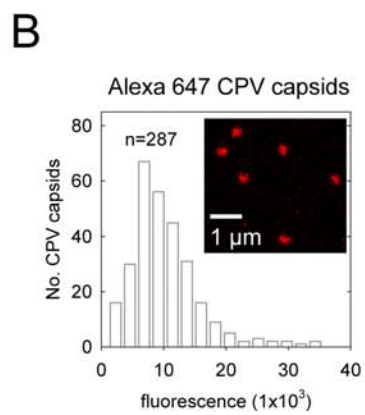
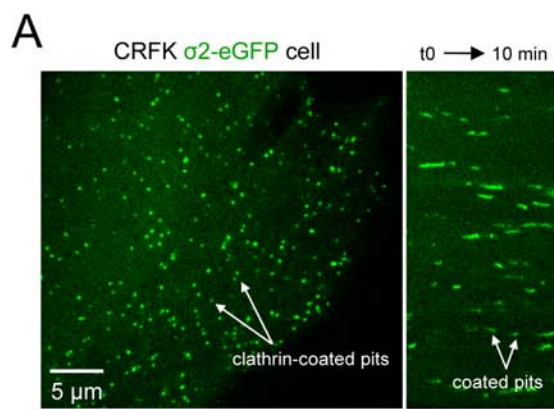
845 (E) Example of receptor engagement by a CPV capsid (Movie S7). TRVb fTfR-eGFP cells were  
846 inoculated with Atto 647 CPV capsids, and images were acquired at 2 s intervals using TIRFM.  
847 Left, images showing attachment of a CPV capsid (red) and the spot of fTfR-eGFP (green, white  
848 arrowheads) that colocalizes with the particle. In each panel, the CPV channel was shifted to the  
849 left by 6 pixels to reveal the underlying receptor signal. Right, plot of the CPV and TfR  
850 fluorescence intensity for the images at left.

851 (F) Box plots showing the fluorescence of Atto 647 CPV capsids or single eGFP molecules on  
852 glass compared to their signals in CPV-fTfR-eGFP complexes on the cell surface. Glass data for  
853 eGFP molecules and CPV are from Figure S2, panels C and D. Cell data are from 76 events

854 observed on 19 cells. Upper and lower bounds of boxes correspond to the 75<sup>th</sup> and 25<sup>th</sup>  
855 percentiles, while error bar whiskers show the 90<sup>th</sup> and 10<sup>th</sup> percentiles of the data. Red and black  
856 horizontal lines indicate the mean and median values of the data sets. The raw fluorescence  
857 intensity of fTfR-eGFP associated with each capsid on the cell surface (middle bar, right panel)  
858 was multiplied by a correction factor of 3.5 (right panel), derived from the difference in the  
859 median fluorescence intensities of capsids on glass compared to those on cells (left panel) due to  
860 the positional loss along the z-axis in the strength of the evanescence field.

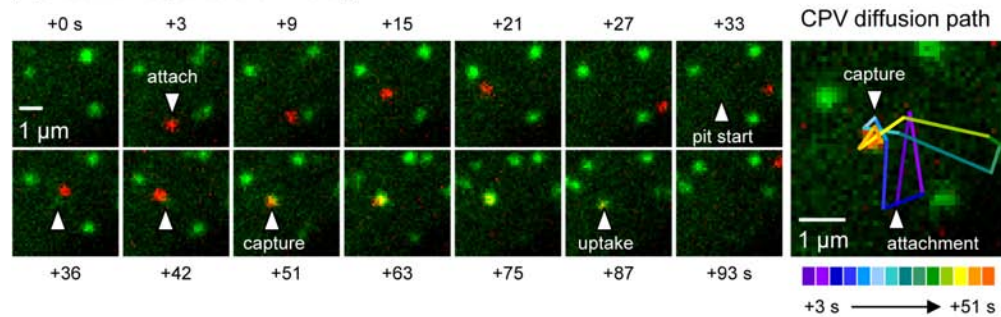
861 **Figure 7. Outcomes of CPV-TfR interactions identified in this study.**

862 CPV capsids (blue) attach to TfRs (orange) on the cell surface. The capsid-receptor complex  
863 diffuses laterally on the cell surface, and at times, capsids engage more than one receptor.  
864 Receptor-bound capsids can diffuse into an assembling clathrin-coated pit (green, AP-2; red,  
865 clathrin), leading to particle endocytosis upon pit scission by dynamin (purple) (Outcome 1).  
866 Alternatively, capsids can detach from TfRs prior to association with a coated pit (Outcome 2).

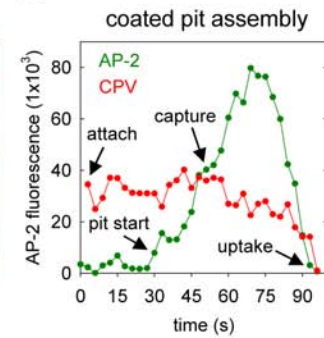




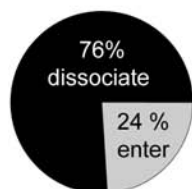
**A** clathrin-dependent CPV entry



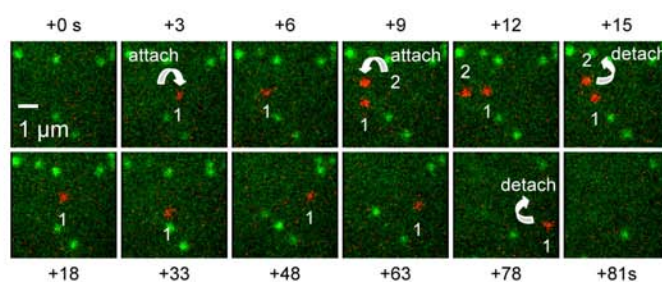
**B**



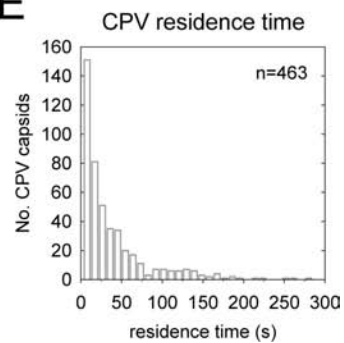
**C** clathrin-dependent entry efficiency (n=628)



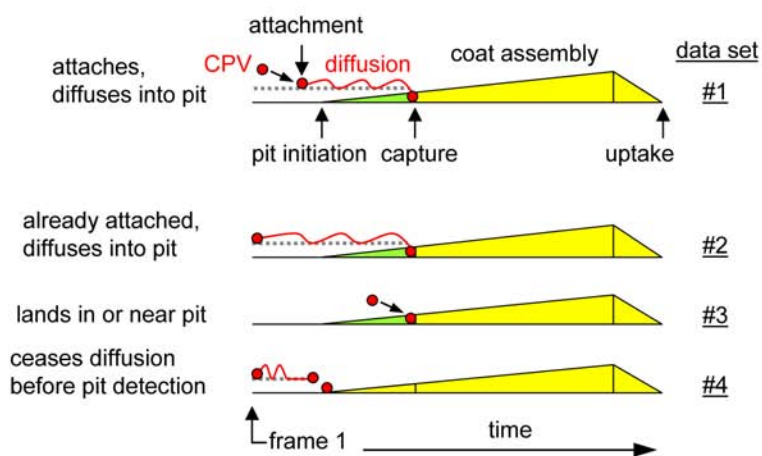
**D** CPV dissociation from cell surface



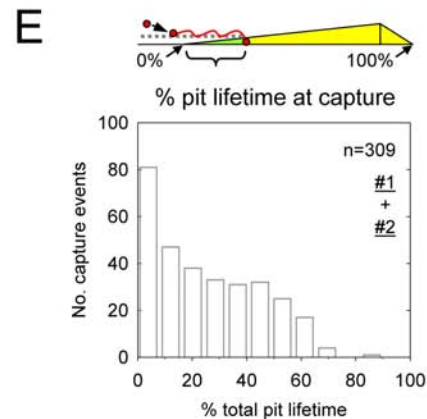
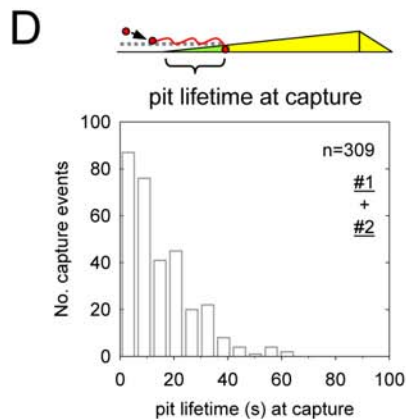
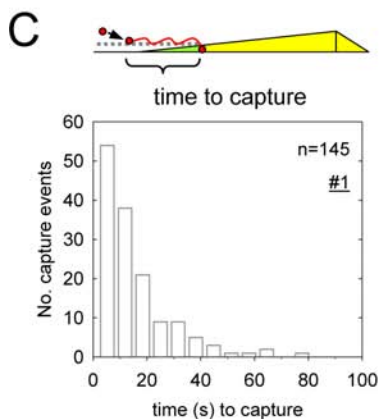
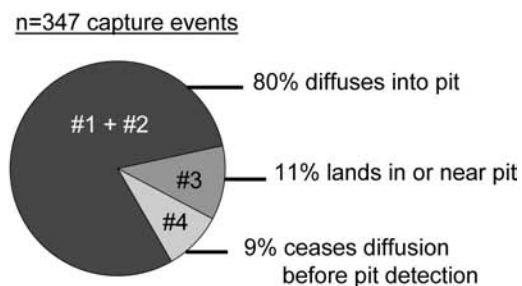
**E**

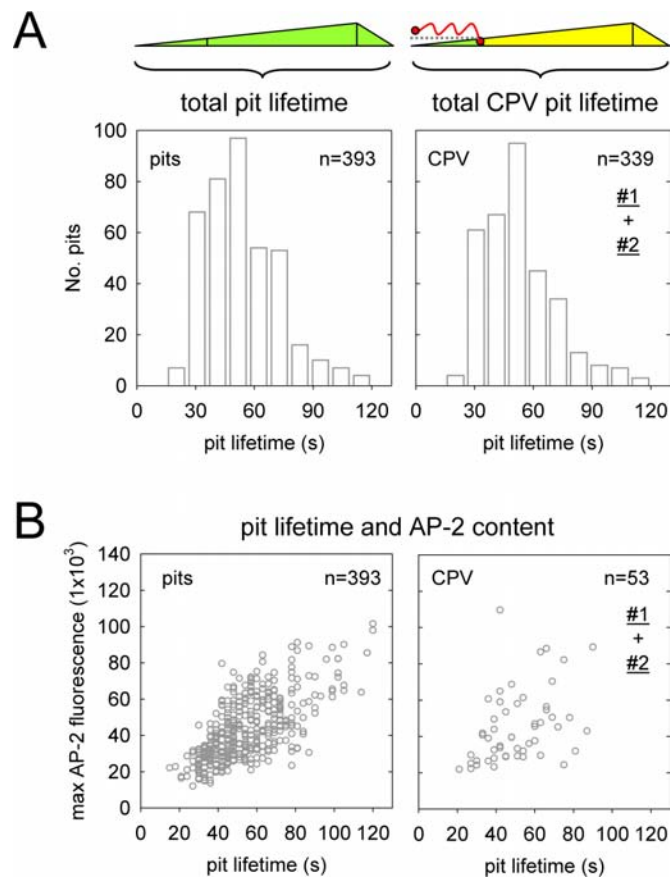


**A** modes of CPV capture by clathrin-coated pits

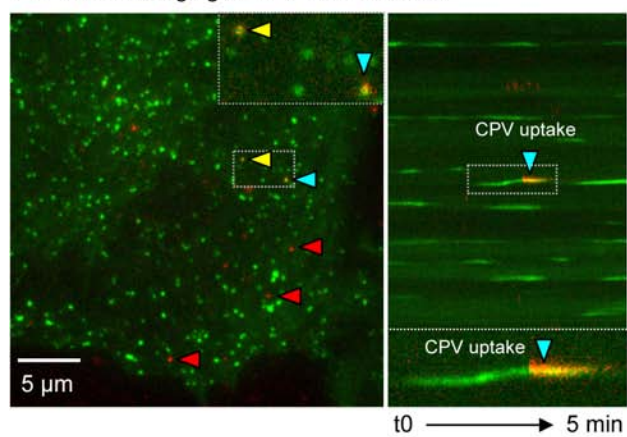


**B** frequency of capture mode usage

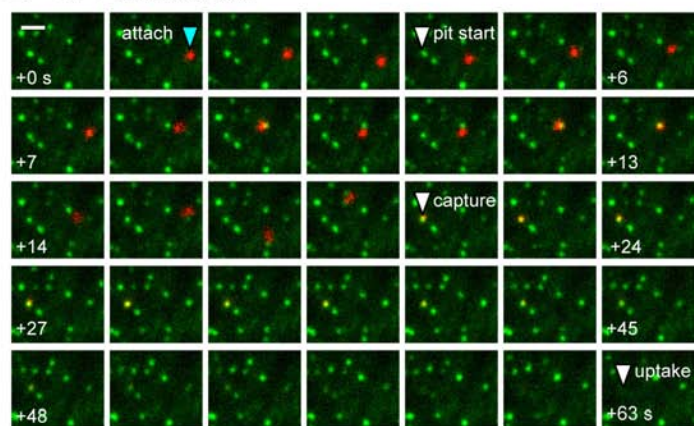




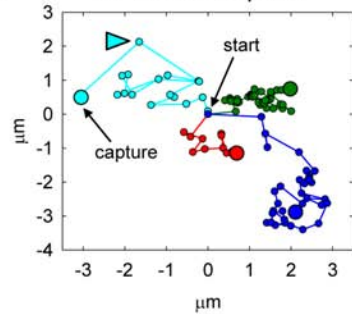
**A** TIRFM imaging of CPV internalization



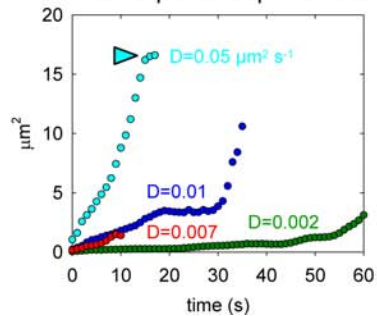
**B** CPV internalization



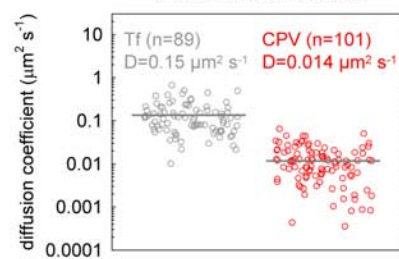
**C** CPV diffusion paths



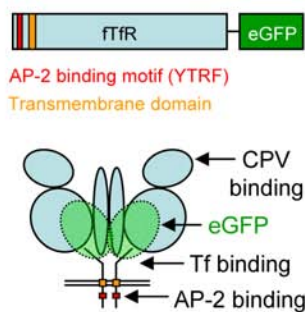
**D** mean squared displacement



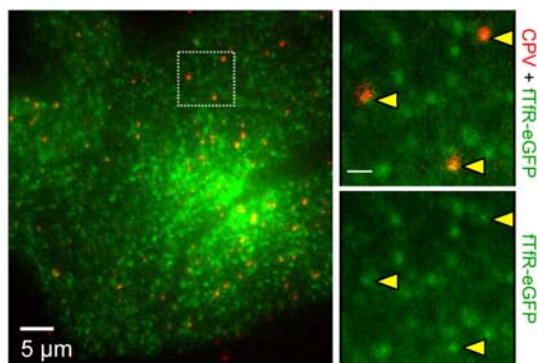
**E** diffusion coefficients



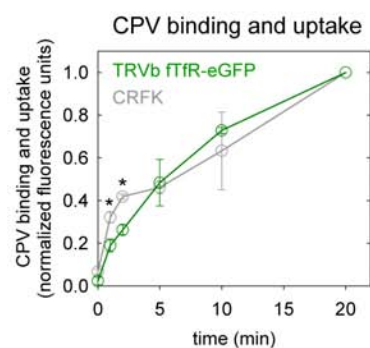
**A** ftfR-eGFP architecture



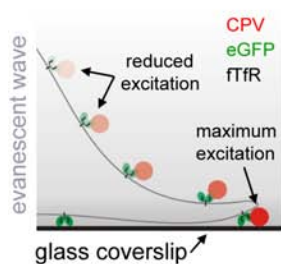
**B** CPV in endosomes of TRVb ftfR-eGFP cells



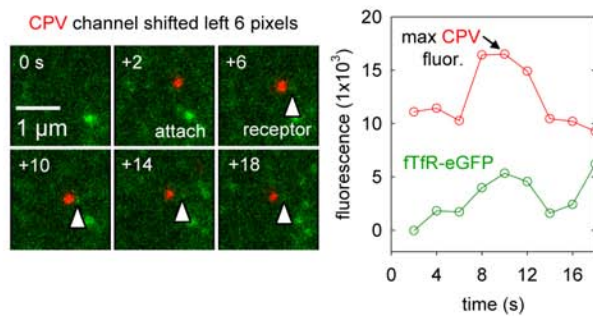
**C**



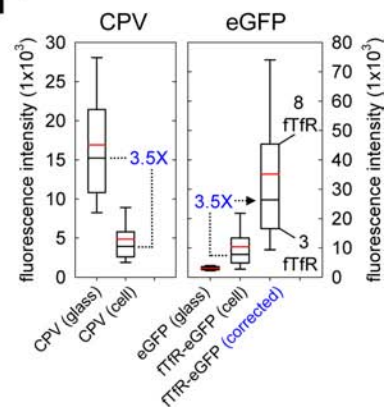
**D** position dependence of CPV detection



**E** CPV-ftfR complex formation



**F**



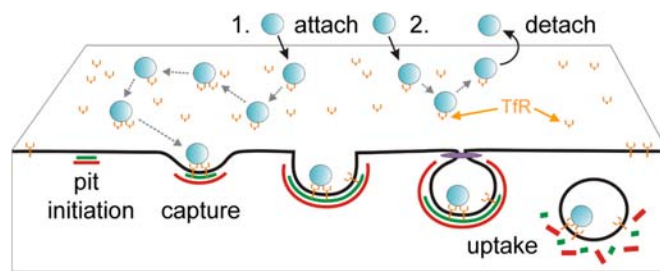


**Table 1. Properties of empty or full CPV capsid entry into CRFK or TRVb cells.**

Cell type	CRFK cells	CRFK cells	CRFK cells	CRFK cells	TRVb <sup>¶</sup> cells
Capsid form	Empty capsids	Full capsids	Empty capsids	Full capsids	Empty capsids
Experiment #	#1	#2	#3	#3	#4
% Entry (total CPV attachments)	24% (n=628, 4 cells)	25% (n=121, 6 cells)	35% (n=54, 3 cells)	25% (n=68, 3 cells)	27% (n=118, 4 cells)
Capture mode as % of (total entry events)	80% diffuse into pit 9% land in/near pit 11% stop diffusing before pit detection (n=347)	80% diffuse into pit 0% land in/near pit 20% stop diffusing before pit detection (n=30)	88% diffuse into pit 0% land in/near pit 12% stop diffusing before pit detection (n=19)	100% diffuse into pit 0% land in/near pit 0% stop diffusing before pit detection (n=17)	95% diffuse into pit 2% land in/near pit 3% stop diffusing before pit detection (n=255)
Average diffusion coefficient	0.014 $\mu\text{m}^2 \text{s}^{-1}$ (n=101)	NT	NT	NT	NT
Time between CPV attachment and capture	15 +/- 14 s (n=145)	*44 +/- 47 s (n=30)	*67 +/- 58 (n=22)	*26 +/- 26 s (n=17)	*23 +/- 19 s (n=51)
Time between pit detection and CPV capture	13 +/- 13 s (n=309)	13 +/- 14 s (n=30)	13 +/- 11 (n=20)	15 +/- 16 s (n=17)	*10 +/- 10 s (n=231)
Time between pit detection and CPV capture (% total pit lifetime)	25 +/- 20 % (n=309)	19 +/- 20 % (n=30)	20 +/- 19 % (n=20)	21 +/- 19 % (n=17)	25 +/- 21 % (n=231)
Total lifetime of CPV pits	53 +/- 19 s (n=339)	*65 +/- 19 s (n=30)	*60 +/- 18 s (n=20)	*63 +/- 27 s (n=17)	*40 +/- 13 s (n=231)
Residence time of capsids that did not enter	39 +/- 44 s (n=463)	*62 +/- 55 s (n=91)	*71 +/- 55 s (n=35)	*60 +/- 46 s (n=51)	46 +/- 27 s (n=71)

¶ TRVb cells expressing fTfR-eGFP

\* indicates statistical significance ( $p < 0.05$ , Student's t-test) relative to corresponding data from experiment #1

# indicates statistical significance ( $p < 0.05$ , Student's t-test) relative to corresponding data from empty capsids in experiments #1 and 3